

Construction of Rotating Sen Black Holes via the Newman-Janis Algorithm and Applications to Accretion Disks and Shadows

Ziqiang Cai,^{1,*} Zhenglong Ban,^{1,†} Qi-Qi Liang,^{1,‡} Haiyuan Feng,^{2,§} and Zheng-Wen Long^{1,¶}

¹*College of Physics, Guizhou University, Guiyang 550025, China*

²*School of Physics and Electronic Engineering, Shanxi Normal University, Taiyuan 030031, China*

In this paper, we derive a rotating Sen black hole (BH) solution from the nonrotating limit static metric of the Sen BH using the Newman-Janis algorithm (NJA) and investigate the thin accretion disk and shadow of the rotating Sen BH. The characteristics of the rotating Sen BH, including its horizon and ergosurface, are analyzed. The results of our analysis indicate that an increase in the effective charge q_m leads to corresponding increases in the energy flux, radiation temperature, and spectral luminosity. It is observed that the BH shadow size decreases with an increase in the parameter q_m . Furthermore, by comparing the theoretically predicted shadow diameters with observational data from M87* and Sgr A*, we constrain the viable range of model parameters. The BH inclination angles are set to 17°, 50° and 90° for the analysis. Our results indicate that, within the constrained parameter space consistent with both M87* and Sgr A*, the shared parameter bounds derived from the rotating Sen BH are given by $0.133158M < q_m < 0.215561M$.

I. INTRODUCTION

The Event Horizon Telescope (EHT) Collaboration has achieved monumental milestones in astrophysics with the first images of supermassive black holes. In April 2019, the EHT released the shadow image of M87*, providing the first direct visual evidence of a black hole's existence [1–6] and confirming their presence in extreme environments. This success was followed by the release of an image of Sgr A* [7], the supermassive BH at the center of our galaxy, in May 2022. Building on these achievements, the EHT has also released polarized images of M87*, further enhancing our understanding of black holes and their surroundings. These observations not only represent significant advancements in observational astronomy but also offer critical tests for theories of gravity under extreme conditions. The physical processes governing BH accretion, a key mechanism driving their observable properties, are intimately linked to the structure of accretion disks around them.

Compact objects such as black holes accumulate mass through accretion, which is facilitated by the presence of an accretion disk. An accretion disk consists of diffuse material like gas and dust that spirals inward toward the central object under the influence of gravitational forces. This process releases gravitational energy in the form of radiation. The foundational model for geometrically thin and optically thick accretion disks was first established by Shakura and Sunyaev. Subsequently, this model was extended to incorporate the effects of general relativity (GR) through the contributions of Page, Novikov, and Thorne [8, 9]. A considerable body of research has explored the physical attributes of matter forming thin accretion disks across different spacetime backgrounds [10–20]. The distinctive features present in the energy flux and the emitted spectrum from these disks provide crucial information about black holes and can also be used to test the validity of modified gravity theories [21]. Complementary to these insights from accretion disk radiation, the geometric signature of black holes—their shadow—offers a unique probe of spacetime geometry under the strongest gravitational fields.

The BH shadow, a two-dimensional dark area observed in the celestial sphere, arises from the strong gravitational influence of the BH. Its shape and dimensions are largely dictated by the specific geometry of the BH spacetime. Thus, strong lensing images and shadows provide an exciting opportunity to both investigate the nature of compact objects and test whether the gravitational field around them conforms to the Schwarzschild or Kerr geometry. The shadow of a Schwarzschild BH was investigated by Synge [22] and Luminet [23]. Meanwhile, Bardeen explored the shadow cast by a Kerr BH [24]. Studies have also explored the shadows cast by a range of other black holes [25–48].

Deriving exact rotating BH solutions from the Einstein field equations is highly challenging due to the complexity of the resulting nonlinear, coupled partial differential equations. The NJA offers a valuable alternative, enabling the construction of stationary, axisymmetric rotating BH spacetimes from static, spherically symmetric seed metrics [49]. Compared to static counterparts, rotating black holes introduce frame-dragging and modify spacetime curvature, profoundly affecting both photon trajectories (shaping shadows) and energy distributions in accretion disks.

The Sen BH, introduced by Sen in the context of superstring theory, provides a specific solution to general relativity that incorporates the effects of electromagnetic fields and scalar fields. Unlike classical black holes (e.g., Schwarzschild and Kerr

* gs.zqcai24@gzu.edu.cn

† gs.zlban22@gzu.edu.cn

‡ 13985671614@163.com

§ Corresponding author; fenghaiyuanphysics@gmail.com

¶ Corresponding author; zwlong@gzu.edu.cn

BHs) characterized solely by mass, angular momentum, and charge, the Sen BH embodies quantum gravitational effects from string theory, making it a pivotal model for exploring quantum phenomena in extreme gravitational fields. Influenced by unique properties such as dilaton and axion fields, its spacetime curvature differs fundamentally from that of Schwarzschild black holes. In the study of Sen black holes, electromagnetic charges differ from those in classical electromagnetism by incorporating effects from both electromagnetic fields and the dilaton field, modifying traditional electric and magnetic interactions to reflect additional dimensions and spacetime curvature effects. This underscores the need for an expanded theoretical framework beyond classical theories when analyzing complex BH dynamics.

In previous studies [50], the shadows of static Sen black holes were explored, showing that their characteristics are closely linked to parameters like mass and charge—for instance, an increase in charge reduces the shadow size. As a solution to the low-energy effective field equations of heterotic string theory, the rotating Sen BH incorporates electromagnetic, dilaton, and Kalb-Ramond fields, making it a unique model to probe quantum gravitational effects in extreme spacetimes. Its ergosphere and event horizon radii depend on both the spin parameter a and effective charge q_m , differing fundamentally from classical Kerr black holes. To investigate whether the factors influencing the shadow size of rotating Sen black holes align with the static case, this paper examines the shadow characteristics of rotating Sen black holes, aiming to reveal differences between the two scenarios. The study of accretion disks and shadows in rotating Sen BH spacetimes is crucial because rotating solutions incorporate string-theoretic effects that modify frame-dragging and spacetime curvature, while EHT observations of M87* and Sgr A* demand models reconciling shadow geometry with accretion dynamics. Additionally, we analyze the physical properties of thin accretion disks around rotating Sen black holes to explore the impact of rotation on accretion dynamics.

This work uses the NJA to generate rotating Sen BH solutions, aiming to bridge the gap by investigating thin accretion disks and shadows in rotating Sen BH spacetimes. We explore how spin and effective charge q_m jointly influence observable quantities like energy flux, radiation temperature, and shadow size. By comparing with EHT data for M87* and Sgr A*, we constrain the parameter space of rotating Sen black holes, providing insights into string-theoretic effects in extreme gravitational fields.

The structure of this paper is as follows. In Sec. II, we briefly review the Sen BH spacetimes and employ the NJA to construct the corresponding rotating Sen BH solution. We also analyze its horizon structure and ergosurface. In Sec. III, based on the properties of thin accretion disks surrounding these rotating Sen black holes, we examine the radiant energy flux, radiation temperature, and emission spectrum. In Sec. IV, we investigate the geodesic equations of photons to study the shadows cast by these black holes. In Sec. V, we use shadow observables to constrain the parameter q_m using EHT observational data from M87* and Sgr A*. Finally, we present our conclusions in Sec. VI.

II. ROTATING SEN BLACK HOLES

A. Construction of Rotating Sen Black Holes

The Sen BH represents a solution to the low-energy effective field equations of heterotic string theory, characterizing the spacetime geometry in the low-energy limit [51]. Unlike classical black holes, the Sen solution exhibits a complex structure embedded in string theoretical frameworks, offering a more comprehensive description of BH physics beyond general relativity. The geometric configuration of this BH is governed by the following line element:

$$ds^2 = -f(r)dt^2 + \frac{1}{g(r)}dr^2 + r^2(d\theta^2 + \sin^2\theta d\phi^2). \quad (2.1)$$

The metric function for this configuration, first derived by Sen in Ref. [52] as a rotating BH solution, is given in the nonrotating limit by

$$\begin{aligned} f(r) &= 1 - \frac{2M}{r + \frac{q_m^2}{M}}, \\ g(r) &= 1 - \frac{2M}{r + \frac{q_m^2}{M}}. \end{aligned} \quad (2.2)$$

Here, M is the BH mass, and q_m denotes an effective charge—encompassing both the electric charge and a dilaton-field-associated effective charge—measured by a static observer at infinity, serving to characterize the specific hair of the BH. Notably, the Sen BH metric reduces to the Schwarzschild metric when $q_m = 0$.

By employing the NJA [49], we derive the metric of a rotating Sen BH, formulated in Boyer–Lindquist coordinates. The

resulting line element is expressed as:

$$\begin{aligned}
ds^2 &= -g_{tt}dt^2 + g_{rr}dr^2 + g_{\theta\theta}d\theta^2 + g_{\phi\phi}d\phi^2 + 2g_{t\phi}dt d\phi \\
&= -\left(1 - \frac{2\tilde{M}r}{\rho^2}\right)dt^2 + \frac{\rho^2}{\Delta}dr^2 + \rho^2d\theta^2 + \frac{\Sigma \sin^2\theta}{\rho^2}d\phi^2 \\
&\quad - \frac{4a\tilde{M}r \sin^2\theta}{\rho^2}dt d\phi.
\end{aligned} \tag{2.3}$$

where

$$\begin{aligned}
\tilde{M} &= \frac{M^2r}{q_m^2 + Mr}, \\
\rho^2 &= r^2 + a^2 \cos^2\theta, \\
\Delta &= a^2 + r^2 \left(1 - \frac{2M^2}{q_m^2 + Mr}\right), \\
\Sigma &= (a^2 + r^2)^2 - a^2 \sin^2\theta \left(a^2 + r^2 \left(1 - \frac{2M^2}{q_m^2 + Mr}\right)\right).
\end{aligned} \tag{2.4}$$

Here, a is the spin parameter of the BH. In the limiting cases, the above spacetime metrics correspond to the standard Kerr BH (with $q_m \rightarrow 0$) and Schwarzschild BH (with $q_m \rightarrow 0$ and $a \rightarrow 0$) in general relativity.

B. Properties of the rotating Sen black hole

Next, we investigate the physical properties of rotating Sen black holes. The horizons of rotating Sen black holes are determined by the condition $g^{rr} = 0$, which yields the following expression:

$$\Delta = a^2 + r^2 \left(1 - \frac{2M^2}{q_m^2 + Mr}\right) = 0. \tag{2.5}$$

The horizon radii are determined by the roots of Eq. (2.5), which exhibit significant sensitivity to the parameters M , a , and q_m . This equation yields two distinct real roots, corresponding to the inner and outer event horizons, respectively. Figure. 1 illustrates the parameter space ($a/M, q_m/M$) for rotating Sen black holes, indicating the region in which physically viable BH solutions exist. The blue solid line represents the extremal limit of BH configurations, while the light blue region adjacent to it delineates the domain in which BH solutions exist within this parameter space. The two-dimensional surfaces satisfying $g_{tt} = 0$ correspond to the inner and outer ergosurfaces, leading to

$$r^2 \left(1 - \frac{2M^2}{q_m^2 + Mr}\right) + a^2 \cos^2\theta = 0. \tag{2.6}$$

Figures. 2 and 3 depict the behavior of the outer horizon and outer ergosurface for various parameter values. In these figures, a blue circle indicates the static case where $a = 0$. It is evident that the shape of the outer ergosphere changes with the spin parameter a , while the size of the outer horizon decreases as a increases. Furthermore, for a fixed value of a , both the radii of the outer ergosphere and outer horizon decrease as q_m increases.

III. THE PHYSICAL PROPERTIES OF THIN ACCRETION DISKS

In this section, we begin with a brief overview of the physical properties of thin accretion disks as described by the Novikov-Thorne model [53]. Subsequently, we will examine how the parameter q_m influences the energy flux, radiation temperature, and emission spectrum in detail. The following values are adopted for the physical constants and the characteristics of the thin accretion disk in our analysis: $c = 2.997 \times 10^{10} \text{cms}^{-1}$, $M_0 = 2 \times 10^{-6} M_\odot \text{yr}^{-1}$, $1 \text{yr} = 3.156 \times 10^7 \text{s}$, $\sigma_{\text{SB}} = 5.67 \times 10^{-5} \text{ergs}^{-1} \text{cm}^{-2} \text{K}^{-4}$, $h = 6.625 \times 10^{-27} \text{ergs}$, $k_B = 1.38 \times 10^{-16} \text{ergK}^{-1}$, $M_\odot = 1.989 \times 10^{33} \text{g}$, and the mass of BH $M = 2 \times 10^6 M_\odot$. In the equatorial plane ($\theta = \pi/2$), we analyze the geodesics of radial timelike particles. The corresponding Lagrangian is expressed as:

$$\mathcal{L} = -g_{tt}\dot{t}^2 + 2g_{t\phi}\dot{t}\dot{\phi} + g_{rr}\dot{r}^2 + g_{\phi\phi}\dot{\phi}^2, \tag{3.1}$$

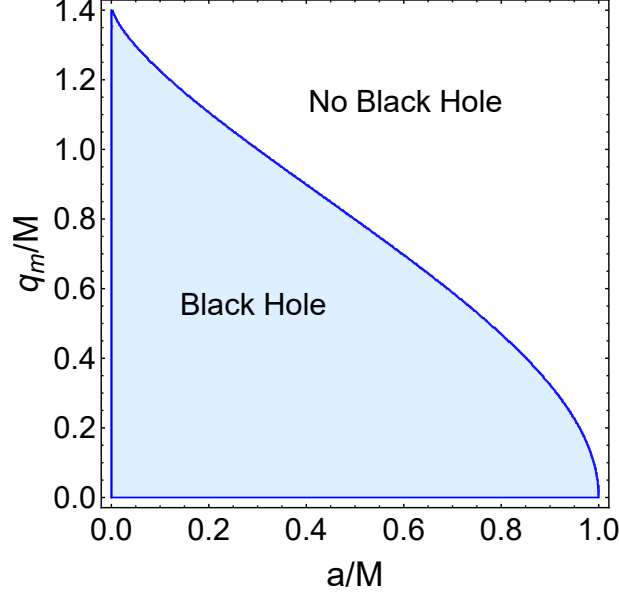


FIG. 1: Regions of BH horizon existence in the $(a/M, q_m/M)$ parameter space.

here, a dot indicates differentiation with respect to the affine parameter τ . Based on the Euler-Lagrange equation ($\frac{d}{d\tau}(\frac{\partial L}{\partial \dot{x}}) - \frac{\partial L}{\partial x} = 0$), for variables $x = t, \phi$, it follows that

$$\begin{aligned} -g_{tt}\dot{t} + g_{t\phi}\dot{\phi} &= -E, \\ g_{t\phi}\dot{t} + g_{\phi\phi}\dot{\phi} &= L. \end{aligned} \quad (3.2)$$

The constants E and L represent the specific energy and angular momentum of particles moving in circular orbits around compact objects. By solving the aforementioned equations, we obtain the four-velocity components of the orbiting particles as follows:

$$\begin{aligned} \dot{t} &= \frac{Eg_{\phi\phi} + Lg_{t\phi}}{g_{t\phi}^2 - g_{tt}g_{\phi\phi}}, \\ \dot{\phi} &= -\frac{Eg_{t\phi} + Lg_{tt}}{g_{t\phi}^2 - g_{tt}g_{\phi\phi}}. \end{aligned} \quad (3.3)$$

Based on the normalization condition $g_{\mu\nu}\dot{x}^\mu\dot{x}^\nu = -1$, it follows that

$$g_{rr}\dot{r}^2 = V_{eff}. \quad (3.4)$$

The effective potential takes the form

$$V_{eff} = -1 + \frac{E^2g_{\phi\phi} + 2ELg_{t\phi} + L^2g_{tt}}{g_{t\phi}^2 - g_{tt}g_{\phi\phi}}. \quad (3.5)$$

In the equatorial plane ($\theta = \frac{\pi}{2}$), circular orbits are identified by the requirements $V_{eff}(r) = 0$ and $V_{eff,r}(r) = 0$. These constraints allow us to express the specific energy E and specific angular momentum L in terms of the particles' angular velocity Ω .

$$\Omega = -\frac{d\phi}{dt} = \frac{-g_{t\phi,r} + \sqrt{(g_{t\phi,r})^2 - g_{tt,r}g_{\phi\phi,r}}}{g_{\phi\phi,r}}, \quad (3.6)$$

$$E = -\frac{g_{tt} + g_{t\phi}\Omega}{\sqrt{-g_{tt} - 2g_{t\phi}\Omega - g_{\phi\phi}\Omega^2}}, \quad (3.7)$$

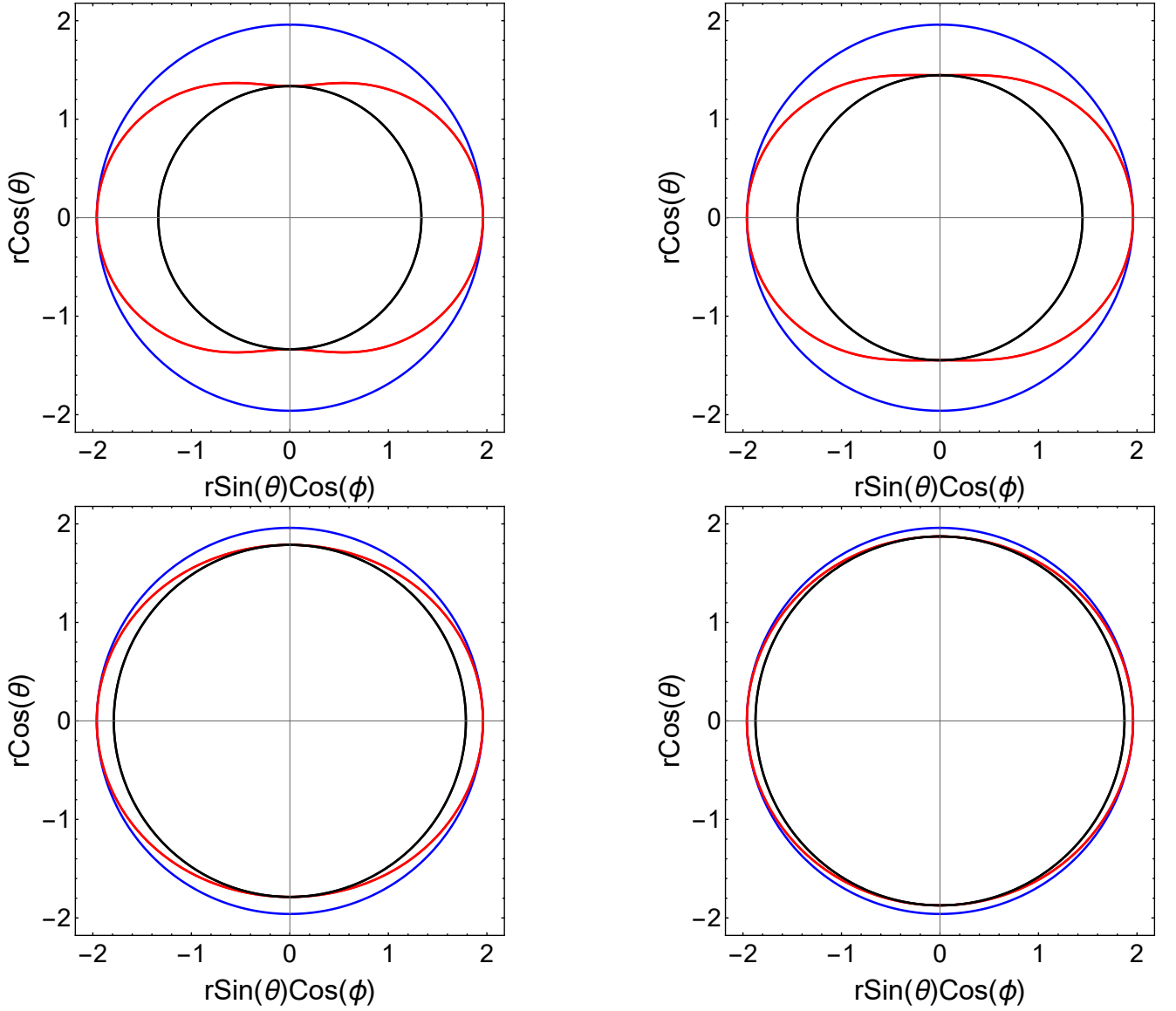


FIG. 2: The shapes of the outer horizon (black solid line) and outer ergosphere (red solid line) are compared to the outer event horizon in the static case (blue solid line) $M = 1$ and $q_m = 0.2$, across various values of a . Specifically, the panels show: Upper left: $a = 0.9$; Upper right: $a = 0.85$; Bottom left: $a = 0.55$; Bottom right: $a = 0.4$.

$$L = \frac{g_{t\phi} + g_{\phi\phi}\Omega}{\sqrt{-g_{tt} - 2g_{t\phi}\Omega - g_{\phi\phi}\Omega^2}}. \quad (3.8)$$

To establish the inner edge of the disk, we need to compute the innermost stable circular orbit (ISCO) of the BH potential based on the condition $V_{eff,rr}(r) = 0$. This condition leads to the following relation:

$$E^2 g_{\phi\phi,rr} + 2ELg_{t\phi,rr} + L^2 g_{tt,rr} - (g_{t\phi}^2 - g_{tt}g_{\phi\phi})_{,rr} = 0. \quad (3.9)$$

The radius r_{isco} marks the inner edge of the thin accretion disk, as equatorial circular orbits for $r < r_{isco}$ are unstable.

Next, we investigate the accretion processes in thin disks surrounding rotating Sen black holes. The emission of radiation flux from the accretion disk's surface is determined through three fundamental structure equations, which include the conservation laws for rest mass, energy, and angular momentum of the particles within the disk [9, 53].

$$F(r) = -\frac{\dot{M}_0 \Omega_r}{4\pi \sqrt{-g}(E - \Omega L)^2} \int_{r_{isco}}^r (E - \Omega L)L_r dr. \quad (3.10)$$

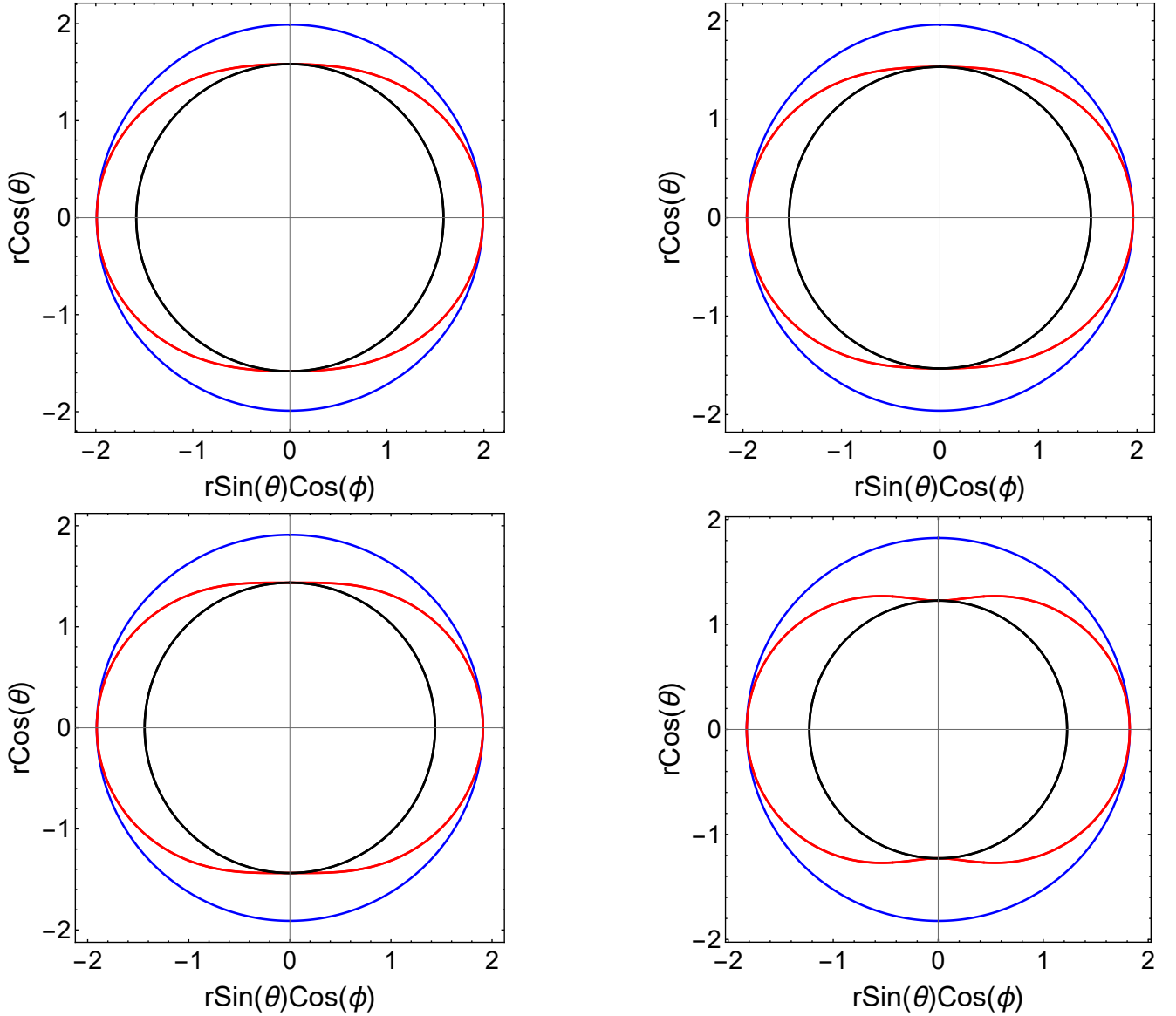


FIG. 3: The shapes of the outer horizon (black solid line) and outer ergosphere (red solid line) are compared to the outer event horizon in the static case (blue solid line) for $M = 1$ and $a = 0.8$, across various values of q_m . Specifically, the panels show: Upper left: $q_m = 0.1$; Upper right: $q_m = 0.2$; Bottom left: $q_m = 0.3$; Bottom right: $q_m = 0.42$.

The equation is commonly used in the literature for cylindrical coordinates. However, for applications in spherical coordinates, it must be reformulated as detailed in [54]

$$F(r) = -\frac{-c^2 \dot{M}_0 \Omega_r}{4\pi \sqrt{-g/g_{\theta\theta}}(E - \Omega L)^2} \int_{r_{isco}}^r (E - \Omega L) L_r dr, \quad (3.11)$$

where \dot{M}_0 stands for the mass accretion rate, g refers to the metric determinant. Figure 4 displays the radial profile of the energy flux $F(r)$ emitted from the accretion disk surrounding a rotating Sen BH, for various values of the parameter q_m . The results indicate that the energy flux generally rises with radius, reaches a maximum, and subsequently declines. For fixed values of the spin parameter a , the energy flux $F(r)$ increases as the parameter q_m increases. Additionally, for a given value of q_m , the peak value of the energy flux $F(r)$ decreases with increasing a .

Within the Novikov-Thorne model framework, the accreted material reaches a state of thermodynamic equilibrium, which implies that the radiation emitted by the disk closely resembles that of a perfect black body. The relationship between the disk's radiation temperature $T(r)$ and its energy flux $F(r)$ is given by the Stefan-Boltzmann law: $F(r) = \sigma_{SB} T^4(r)$, where σ_{SB} represents the Stefan-Boltzmann constant. Figure 5 depicts the radiation temperature on the disk surface for different values

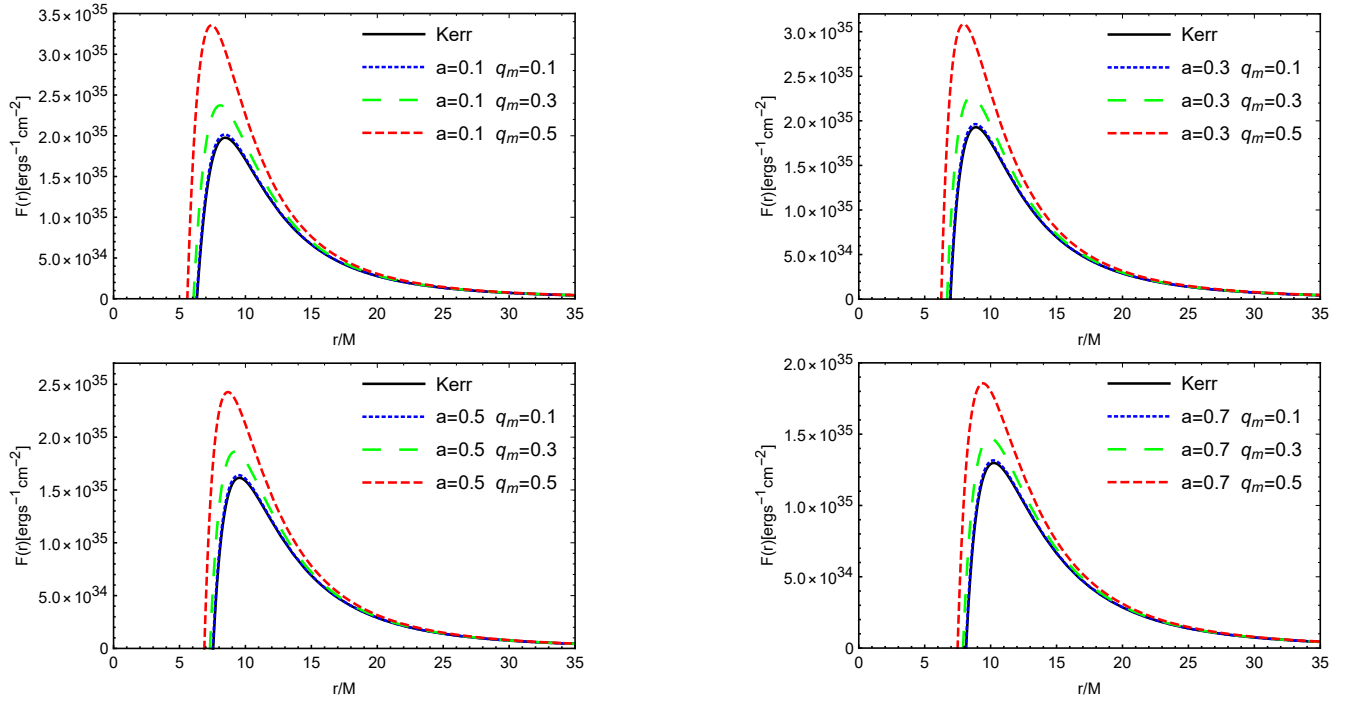


FIG. 4: The energy flux $F(r)$ emitted from an accretion disk surrounding a rotating Sen BH is shown for various values of the parameter q_m . Panels correspond to spin parameters $a = 0.1$ (top-left), $a = 0.3$ (top-right), $a = 0.5$ (bottom-left), and $a = 0.7$ (bottom-right). The black line represents the radiation scenario for the Kerr BH.

of the parameters. Similar to case of the energy flux, the radiation temperature $T(r)$ exhibits a characteristic radial profile: it initially increases with radius, peaks at an intermediate distance, and then decreases. For fixed values of the spin parameter a , higher values of q_m lead to an overall increase in $T(r)$. However, for a fixed q_m , the peak temperature diminishes as a increases.

The red-shifted black body spectrum of the observed luminosity $L(\nu)$ for a thin accretion disk around a BH is provided in [55]

$$L(\nu) = 4\pi d^2 I(\nu) = \frac{8\pi h \cos \gamma}{c^2} \int_{r_i}^{r_f} \int_0^{2\pi} \frac{\nu_e^3 r}{e^{h\nu_e/k_B T} - 1} dr d\phi, \quad (3.12)$$

where, d represents the distance to the disk center, $I(\nu)$ denotes the thermal energy flux radiated by the disk, h is the Planck constant, k_B is the Boltzmann constant, and γ is the disk inclination angle, which we will set to zero. The quantities r_f and r_i correspond to the outer and inner radii of the disk's edges, respectively. Assuming that the energy flux emitted from the disk surface vanishes at r_f , we select $r_i = r_{isco}$ and $r_f \rightarrow \infty$ for calculating the luminosity $L(\nu)$ of the disk. The emitted frequency is given by $\nu_e = \nu(1+z)$, where the redshift factor z can be expressed as follows:

$$1+z = \frac{1 + \Omega r \sin \gamma \sin \phi}{\sqrt{-g_{tt} - 2g_{t\phi}\Omega - g_{\phi\phi}\Omega^2}}, \quad (3.13)$$

where the light bending is neglected [23, 56]. The variations of spectral energy distribution are illustrated in Fig. 6. Figure 6 illustrates the variations in the spectral energy distribution, which follow a similar trend to those observed in the energy flux and disk temperature.

IV. NULL GEODESIC EQUATIONS AND BLACK HOLE SHADOW

To determine the shape of the shadow cast by a rotating Sen BH, we initially examine the null geodesics in this spacetime geometry. Utilizing the Hamilton-Jacobi equation, we analyze the null geodesic structure of the rotating Sen BH, as outlined below [57]

$$\frac{\partial S}{\partial \tau} = -\frac{1}{2} g^{\mu\nu} \frac{\partial S}{\partial x^\mu} \frac{\partial S}{\partial x^\nu}. \quad (4.1)$$

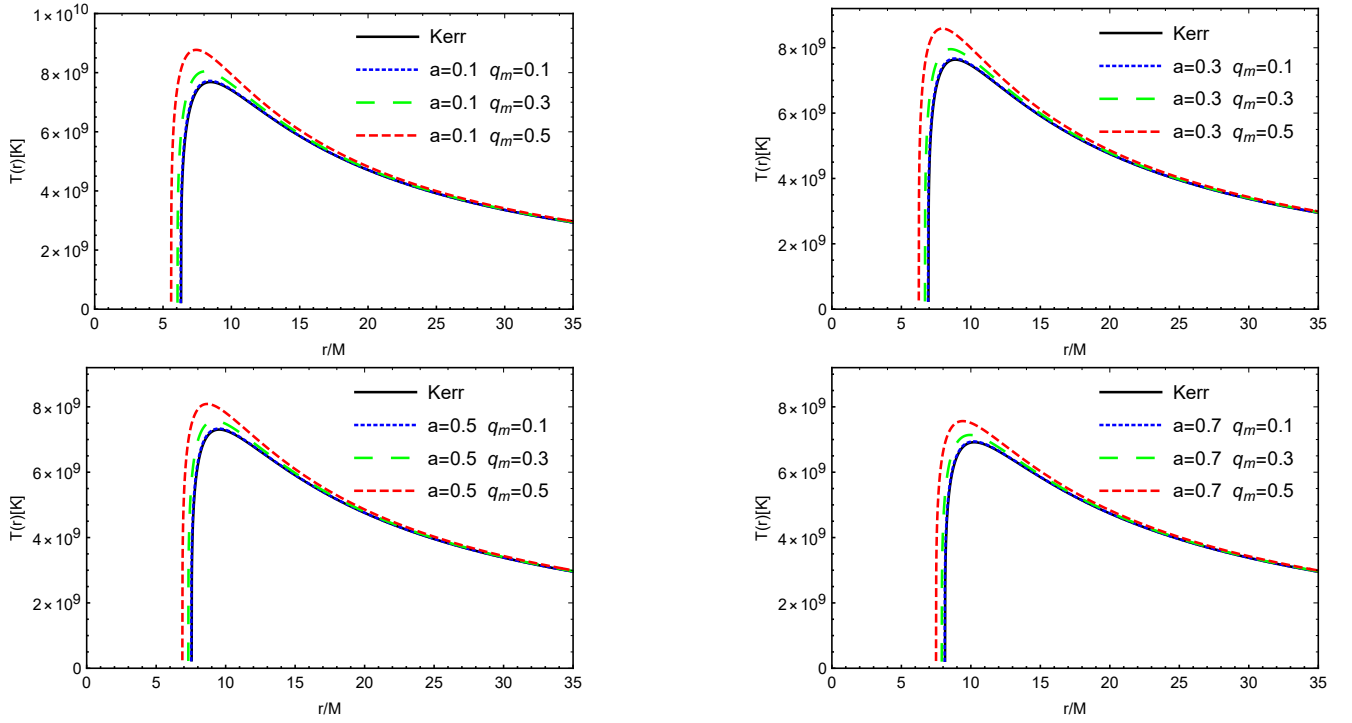


FIG. 5: The temperature $T(r)$ of an accretion disk around a rotating Sen BH is shown for various values of the parameter q_m . Panels correspond to spin parameters $a = 0.1$ (top-left), $a = 0.3$ (top-right), $a = 0.5$ (bottom-left), and $a = 0.7$ (bottom-right). The black line represents the radiation scenario for the Kerr BH.

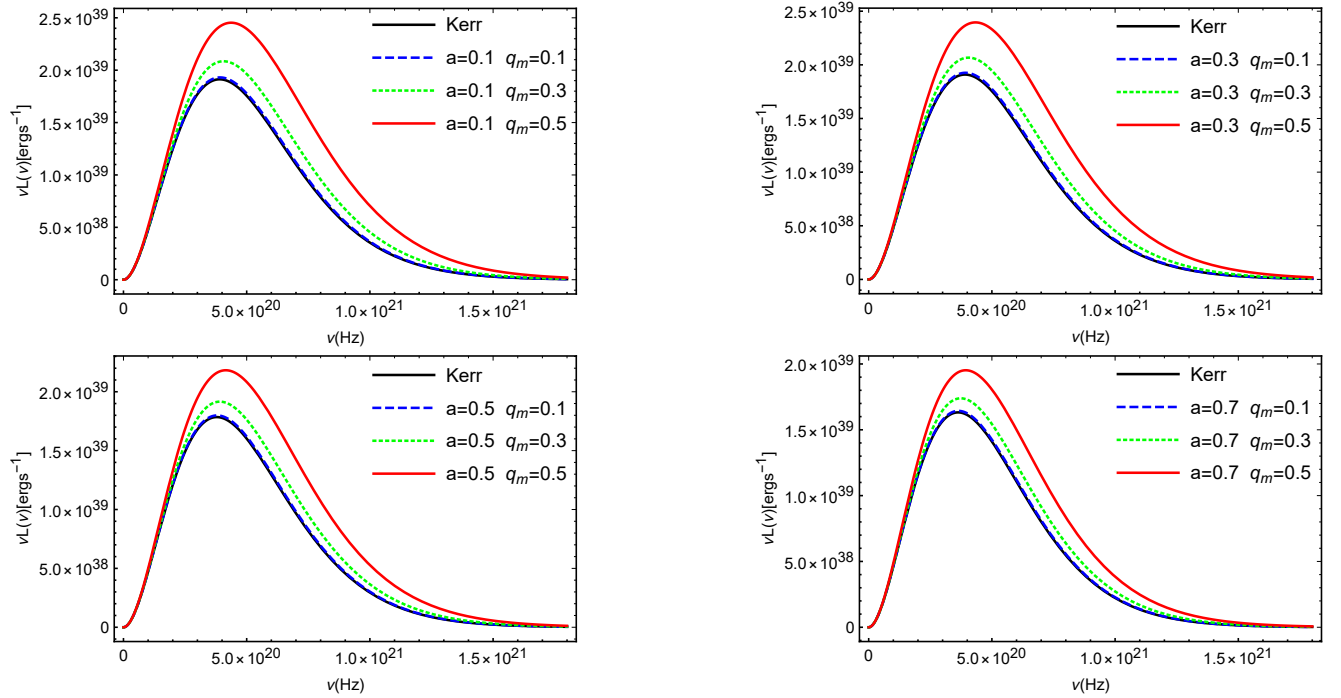


FIG. 6: The emission spectrum $vL(v)$ of the accretion disk surrounding a rotating Sen BH is displayed for various values of the parameter q_m . Panels correspond to spin parameters $a = 0.1$ (top-left), $a = 0.3$ (top-right), $a = 0.5$ (bottom-left), and $a = 0.7$ (bottom-right). The black solid line represents the corresponding spectrum for the Kerr BH.

Here, τ represents an affine parameter along the geodesics, and S is the Jacobi action. The Jacobi action S can be expressed in the following separable form:

$$S = \frac{1}{2}m^2\tau - Et + L\phi + S_r(r) + S_\theta(\theta). \quad (4.2)$$

Here, m represents the mass of the particle moving within the BH spacetime, and for a photon, $m = 0$. The two functions S_r and S_θ depend solely on r and θ , respectively. Combining Eq. (4.1) with Eq. (4.2), we can formulate the geodesic equations as follows:

$$\rho^2 \frac{dt}{d\tau} = a(L - aE \sin^2 \theta) + \frac{r^2 + a^2}{\Delta(r)} [(r^2 + a^2)E - aL], \quad (4.3)$$

$$\rho^2 \frac{dr}{d\tau} = \sqrt{R(r)}, \quad (4.4)$$

$$\rho^2 \frac{d\theta}{d\tau} = \sqrt{\Theta(\theta)}, \quad (4.5)$$

$$\rho^2 \frac{d\phi}{d\tau} = \frac{L}{\sin^2 \theta} - aE + \frac{a}{\Delta(r)} [(r^2 + a^2)E - aL], \quad (4.6)$$

where

$$R(r) = ((r^2 + a^2)E - aL)^2 - \Delta(r)(C + (L - aE)^2), \quad (4.7)$$

$$\Theta(\theta) = C + (a^2E^2 - L^2 \csc^2 \theta) \cos^2 \theta, \quad (4.8)$$

with, C is the Carter constant [57].

The behavior of a photon's motion is defined by the two impact parameters

$$\xi = \frac{L}{E}, \quad \eta = \frac{C}{E^2}. \quad (4.9)$$

To ascertain the shape of the BH shadow, we need to calculate the critical circular orbit for photons, based on the unstable condition

$$R(r)|_{r=r_{ps}} = \frac{dR(r)}{dr}|_{r=r_{ps}} = 0, \quad \frac{d^2R(r)}{dr^2}|_{r=r_{ps}} > 0, \quad (4.10)$$

here, r_{ps} denotes the radius of the unstable circular photon orbits. Solving Eq. (4.10) provides the critical values of the impact parameters (ξ, η) for unstable orbits, which are given by:

$$\xi = \frac{a^2 + r_{ps}^2 - \frac{4\Delta(r_{ps})r_{ps}}{\Delta'(r_{ps})}}{a}, \quad (4.11)$$

$$\eta = \frac{-16\Delta(r_{ps})^2 r_{ps}^2 - r_{ps}^4 \Delta'(r_{ps})^2 + 8\Delta(r_{ps})r_{ps}(2a^2 r_{ps} + r_{ps}^2 \Delta'(r_{ps}))}{a^2 \Delta'(r_{ps})^2}. \quad (4.12)$$

To describe the shadow, we utilize the celestial coordinates (X, Y) as follows:

$$X = \lim_{r_0 \rightarrow \infty} \left(-r_0^2 \sin \theta_0 \frac{d\phi}{dr} \Big|_{\theta \rightarrow \theta_0} \right) = -\xi \csc \theta_0, \quad (4.13)$$

$$Y = \lim_{r_0 \rightarrow \infty} \left(r_0^2 \frac{d\theta}{dr} \Big|_{\theta \rightarrow \theta_0} \right) = \pm \sqrt{\eta + a^2 \cos^2 \theta_0 - \xi^2 \cot^2 \theta_0}, \quad (4.14)$$

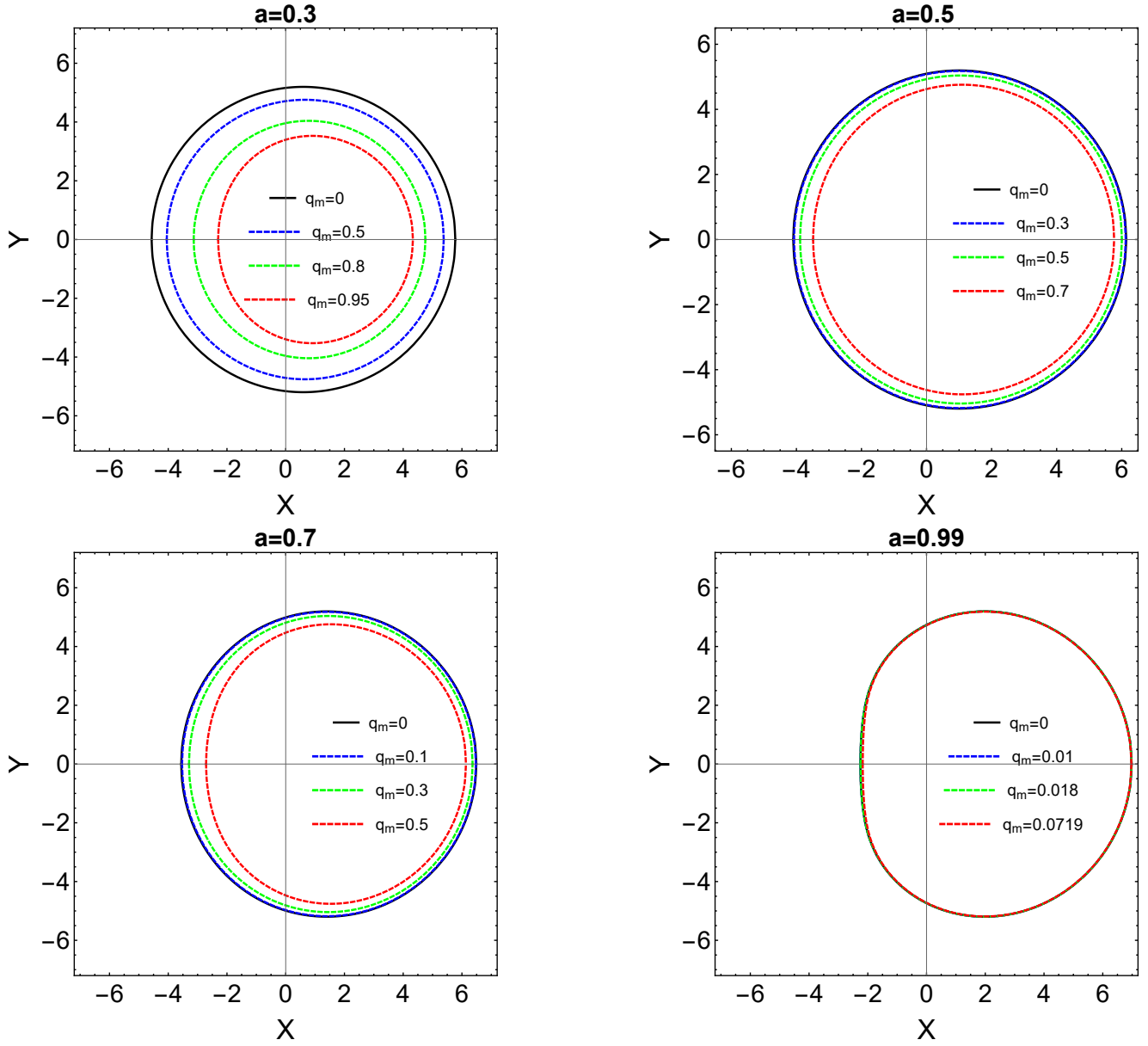


FIG. 7: The shadows cast by rotating Sen black holes vary with the parameters a and q_m .

where r_0 is the distance between the observer and the BH, and θ_0 is the inclination angle between the observer's line of sight and the rotational axis of the BH. In the particular case where the observer is situated on the black hole's equatorial plane with $\theta_0 = \pi/2$, we obtain:

$$X = -\xi, \quad Y = \pm \sqrt{\eta}. \quad (4.15)$$

Figure 7 illustrates the shadows of rotating Sen black holes for various selected values of the spin parameter a and the parameter q_m . The black solid line represents the boundary of the shadow cast by a Kerr BH ($q_m = 0$). The rotating Sen black holes shadows are not perfect circles. It is found that, for a fixed spin parameter a , the size of the BH shadow diminishes with increasing q_m . When $a = 0.99$, the shape of the BH shadow appears D-shaped. Let us now shift our focus to the actual size and distortion of the shadow cast by a rotating Sen BH. We introduce two observables that serve to characterize the BH shadow: R_s and δ_s . Specifically, the parameter R_s denotes the actual size of the shadow, whereas δ_s represents the distortion in the shadow's shape. These parameters will allow for a more detailed analysis of the black hole's shadow within the context of its observable characteristics. To determine the radius R_s , we use three points on the shadow boundary: the top point (x_t, y_t) , the bottom point

(x_b, y_b) , and the rightmost point $(x_r, 0)$. As defined in [58]:

$$R_s = \frac{(x_r - x_l)^2 + y_l^2}{2(x_r - x_l)}. \quad (4.16)$$

The deformation δ_s , describing how the shadow's shape deviates from a standard circle, is defined in [58] as:

$$\delta_s = \frac{D}{R_s} = \frac{|x_l - \tilde{x}_l|}{R_s}. \quad (4.17)$$

Here, D represents the distance between the leftmost point $(x_l, 0)$ of the shadow and the rightmost point $(\tilde{x}_l, 0)$ of the reference circle. The variations in R_s and δ_s for the shadows are depicted in Fig. 8. The parameter q_m significantly affects both the apparent shape and size of the BH shadow. As illustrated in Fig. 8, an increase in q_m leads to a gradual decrease in the shadow's size and a corresponding increase in its distortion.

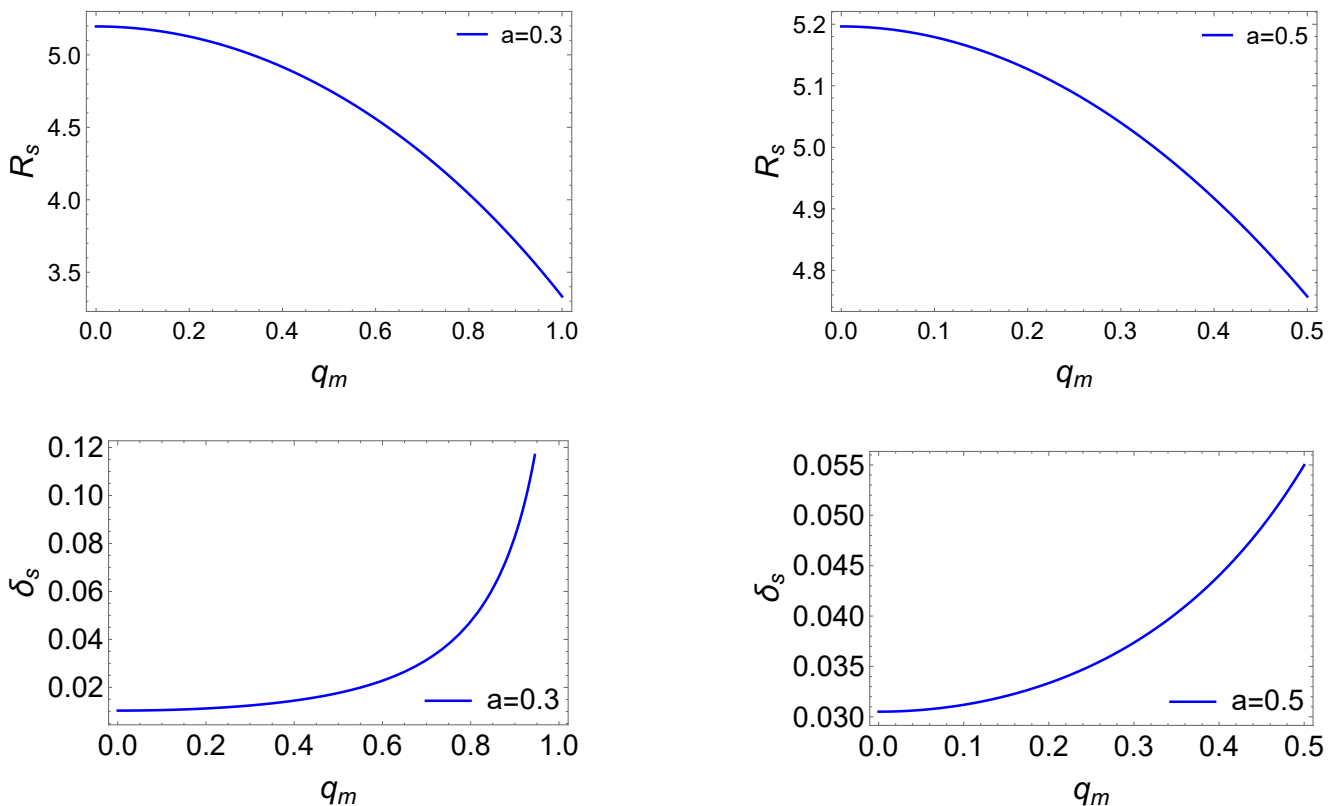


FIG. 8: The variations of R_s and δ_s with respect to q_m for rotating Sen black holes are shown. In the left panel, the spin parameter $a = 0.3$, while in the right panel, $a = 0.5$.

V. CONSTRAINTS FROM THE EHT OBSERVATIONS OF SUPERMASSIVE BLACK HOLES OF M87* AND SGR A*

The EHT observations of M87* and Sgr A* impose significant constraints on theoretical models of black holes. Through imaging the shadows and surrounding emissions of these supermassive black holes, the EHT data allows researchers to refine parameter constraints. Such observations yield unprecedented insights into the characteristics of black holes and their surroundings. In this section, we employ EHT observational data related to the supermassive black holes at M87* and Sgr A* to constrain rotating Sen black holes.

A. Constraints from the EHT results of M87*

An areal radius $R_s = \sqrt{A/\pi}$ defines the BH shadow, which corresponds to an angular diameter θ_d as seen from the observer's celestial sphere:

$$\theta_d = 2 \frac{R_s}{d} = \frac{2}{d} \sqrt{\frac{A}{\pi}}, \quad (5.1)$$

here, A is the BH shadow area, and d represents the distance between the BH and Earth, which is $d = 16.8$ Mpc for M87*. Figure. 9 shows the variation in the shadow angular diameter of rotating Sen black holes with respect to parameters a and q_m , for viewing angles $\theta_0 = 17^\circ$ and $\theta_0 = 90^\circ$. The M87* shadow's angular diameter, constrained within the 1σ bound of $39\mu\text{as} \leq \theta_d \leq 45\mu\text{as}$, imposes limits on the spin parameter a and the parameter q_m based on the inclination angle θ_0 . Specifically, for $\theta_0 = 17^\circ$, we find $0 < a < 0.529574M$ and $0 < q_m < 0.215561M$. When $\theta_0 = 90^\circ$, the constraints are $0 < a < 0.692145M$ and $0 < q_m < 0.215561M$.

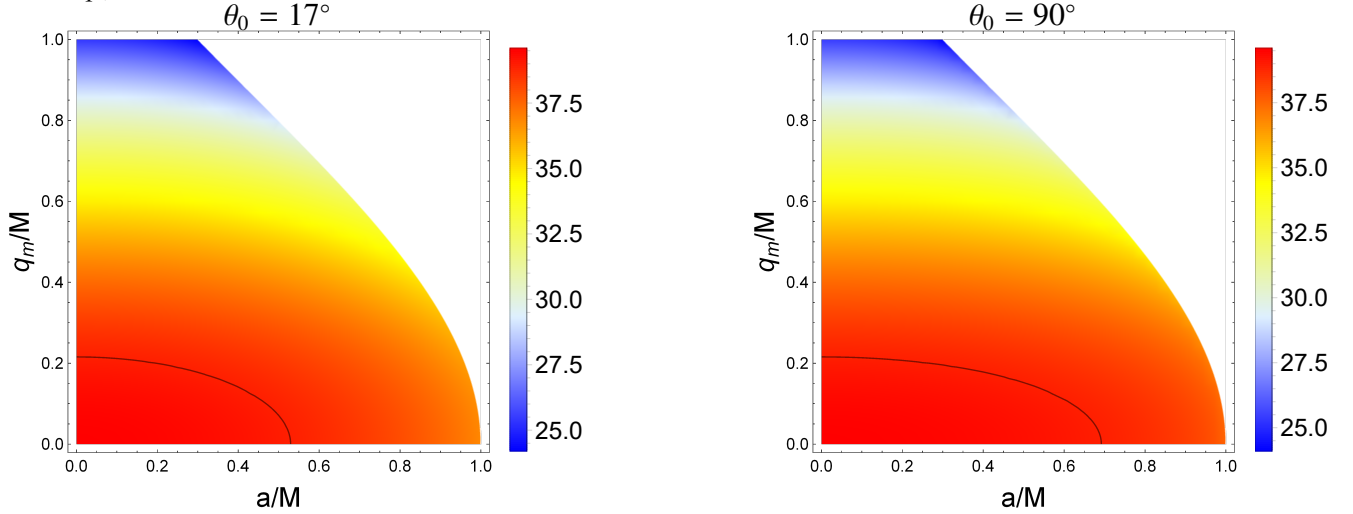


FIG. 9: Density plots of the shadow angular diameter θ_d for rotating Sen black holes are displayed. The left plot is for $\theta_0 = 17^\circ$, and the right one corresponds to $\theta_0 = 90^\circ$. The observed angular diameter of M87* is $\theta_d = 42 \pm 3\mu\text{as}$ within 1σ . The black solid line denotes $\theta_d = 39\mu\text{as}$.

B. Constraints from the EHT results of Sgr A*

Based on the 2017 VLBI observing mission at 1.3 mm wavelength, the EHT collaboration supplied shadow data for the Sgr A* BH. The images of Sgr A*'s shadow are crucial for understanding the properties of astrophysical black holes because: (i) Sgr A* examines a curvature that is 10^6 times greater than that of M87*, and (ii) it employs separate previous estimations for the mass-to-distance ratio. Utilizing various imaging and modeling techniques, these shadow images show remarkable consistency in their characteristics. Based on independent stellar dynamics observations of the S0-2 star's orbit using the Keck Telescopes and the Very Large Telescope Interferometer (VLTI), the mass and distance of Sgr A* are determined to be $M = 4.0^{+1.1}_{-0.6} \times 10^6 M_\odot$ and $D = 8$ kpc. The EHT image of Sgr A* shows an angular shadow diameter within the range $\theta_d \in (46.9, 50)\mu\text{as}$, which is consistent with the expected shadow of a Kerr BH. In Fig. 10, we illustrate the shadow angular diameters of rotating Sen black holes at two viewing angles: $\theta_0 = 50^\circ$ and $\theta_0 = 90^\circ$. The observed angular diameters of Sgr A* are shown with the solid black line representing the maximum value of $50\mu\text{as}$ and the dashed black line indicating the minimum value of $46.9\mu\text{as}$. Specifically, for $\theta_0 = 50^\circ$, the spin parameter a is constrained to $0.403731 < a < 1M$, and the parameter q_m within $0.133158M < q_m < 447632M$. At $\theta_0 = 90^\circ$, the constraints tighten to $0.449765 < a < 1M$ for a and $0.133158M < q_m < 447632M$ for q_m .

VI. CONCLUSION

In this study, we have derived a rotating Sen BH solution by applying the NJA to the spherical symmetric Sen BH. We have further investigated the physical properties of the event horizon and ergosurface associated with rotating Sen black holes. Our

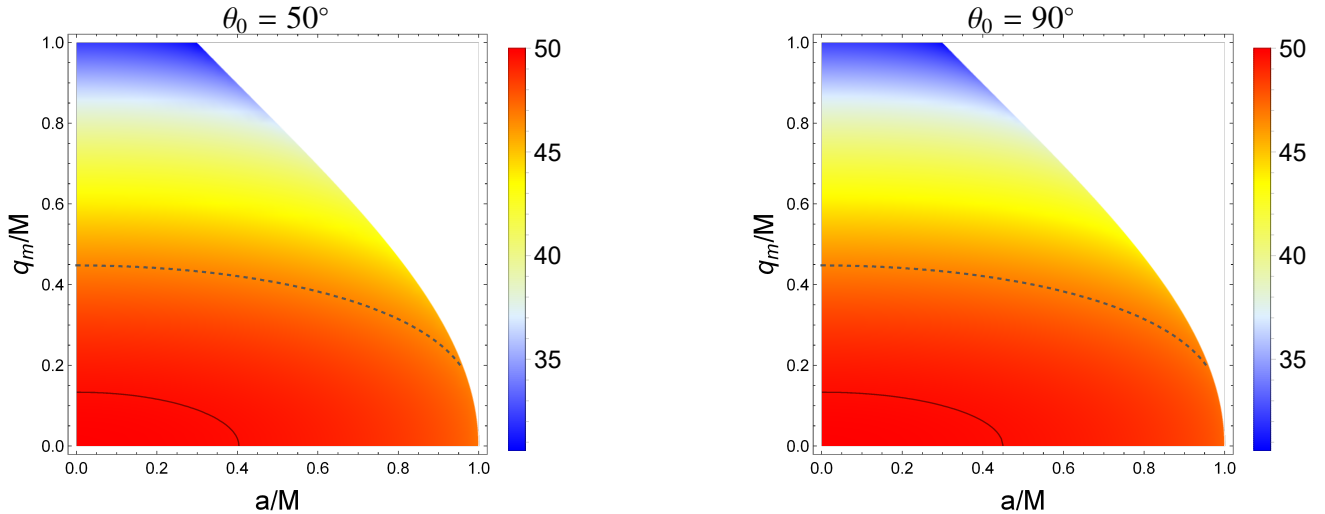


FIG. 10: Density plots of the shadow angular diameter θ_d for rotating Sen black holes at two viewing angles: $\theta_0 = 50^\circ$ (left) and $\theta_0 = 90^\circ$ (right). The solid black line indicates $\theta_d = 50\mu\text{as}$, representing the maximum observed value for Sgr A*, while the dashed black line denotes $\theta_d = 46.9\mu\text{as}$, the minimum observed value.

analysis reveals that the number of horizons is determined by both the effective charge q_m and the spin parameter a . Notably, while the shape of the outer ergosphere is sensitive to variations in a , the size of the outer horizon decreases monotonically with increasing a . Moreover, for a fixed value of the spin parameter, both the radii of the outer horizon and outer ergosphere shrink as q_m increases.

Additionally, the Novikov-Thorne model was employed to analyze the properties of thin accretion disks around rotating Sen black holes. Under specific values of the spin parameter a , the influence of q_m on the energy flux, radiation temperature, and luminosity spectrum of the thin disk has been systematically explored. The results show that the energy flux, radiation temperature, and luminosity spectrum exhibit similar behavior: they initially increase with radius, reach a peak, and then decrease. For a fixed value of the spin parameter a , all three quantities grow as the effective charge q_m increases. Moreover, when q_m is held constant, the peak values of the energy flux, radiation temperature, and luminosity spectrum diminish with increasing a .

Furthermore, we have analyzed how the parameters a and q_m influence both the shape and size of the shadow cast by rotating Sen black holes. The results demonstrate that, for a fixed spin parameter a , the shadow size decreases as q_m increases. Through comparison with EHT observational data for M87* and Sgr A*, we have determined constraints on the parameters of rotating Sen black holes across various inclination angles. The derived bounds indicate that, under the combined observational constraints, the effective charge q_m must lie within the interval $0.133158M < q_m < 0.215561M$. These results confirm that the rotating Sen BH model is consistent with the current high-resolution BH imaging observations, and provide a theoretical basis for further exploring the string-theoretic effects in extreme gravitational fields.

ACKNOWLEDGMENTS

This research was supported by the National Natural Science Foundation of China (Grant No. 12265007).

-
- [1] K. Akiyama *et al.* [Event Horizon Telescope], First M87 Event Horizon Telescope Results. I. The Shadow of the Supermassive Black Hole, *Astrophys. J. Lett.* **875**, L1 (2019), [arXiv:1906.11238 [astro-ph.GA]].
 - [2] K. Akiyama *et al.* [Event Horizon Telescope], First M87 Event Horizon Telescope Results. II. Array and Instrumentation, *Astrophys. J. Lett.* **875**, no.1, L2 (2019), [arXiv:1906.11239 [astro-ph.IM]].
 - [3] K. Akiyama *et al.* [Event Horizon Telescope], First M87 Event Horizon Telescope Results. III. Data Processing and Calibration, *Astrophys. J. Lett.* **875**, no.1, L3 (2019), [arXiv:1906.11240 [astro-ph.GA]].
 - [4] K. Akiyama *et al.* [Event Horizon Telescope], First M87 Event Horizon Telescope Results. IV. Imaging the Central Supermassive Black Hole, *Astrophys. J. Lett.* **875**, no.1, L4 (2019), [arXiv:1906.11241 [astro-ph.GA]].
 - [5] K. Akiyama *et al.* [Event Horizon Telescope], First M87 Event Horizon Telescope Results. V. Physical Origin of the Asymmetric Ring, *Astrophys. J. Lett.* **875**, no.1, L5 (2019), [arXiv:1906.11242 [astro-ph.GA]].
 - [6] K. Akiyama *et al.* [Event Horizon Telescope], First M87 Event Horizon Telescope Results. VI. The Shadow and Mass of the Central Black Hole, *Astrophys. J. Lett.* **875**, no.1, L6 (2019), [arXiv:1906.11243 [astro-ph.GA]].

- [7] K. Akiyama *et al.* [Event Horizon Telescope], First Sagittarius A* Event Horizon Telescope Results. I. The Shadow of the Supermassive Black Hole in the Center of the Milky Way, *Astrophys. J. Lett.* **930**, no.2, L12 (2022), [arXiv:2311.08680 [astro-ph.HE]].
- [8] N. I. Shakura and R. A. Sunyaev, Black holes in binary systems. Observational appearance, *Astron. Astrophys.* **24**, 337-355 (1973), [astro-ph/0301586].
- [9] D. N. Page and K. S. Thorne, Disk-Accretion onto a Black Hole. Time-Averaged Structure of Accretion Disk, *Astrophys. J.* **191**, 499-506 (1974), [astro-ph/0301586].
- [10] T. Harko, Z. Kovacs and F. S. N. Lobo, Testing Hořava-Lifshitz gravity using thin accretion disk properties, *Phys. Rev. D* **80**, no.4, 044021 (2009), [arXiv:0907.1449 [gr-qc]].
- [11] S. Chen and J. Jing, Thin accretion disk around a Kaluza–Klein black hole with squashed horizons, *Phys. Lett. B* **704**, 641-645 (2011), [arXiv:1106.5183 [gr-qc]].
- [12] C. Liu, S. Yang, Q. Wu and T. Zhu, Thin accretion disk onto slowly rotating black holes in Einstein–Æther theory, *JCAP* **02**, no.02, 034 (2022), [arXiv:2107.04811 [gr-qc]].
- [13] M. Heydari-Fard, M. Heydari-Fard and H. R. Sepangi, Thin accretion disks around rotating black holes in 4D Einstein–Gauss–Bonnet gravity, *Eur. Phys. J. C* **81**, no.5, 473 (2021), [arXiv:2105.09192 [gr-qc]].
- [14] R. K. Karimov, R. N. Izmailov, A. Bhattacharya and K. K. Nandi, Accretion disks around the Gibbons–Maeda–Garfinkle–Horowitz–Strominger charged black holes, *Eur. Phys. J. C* **78**, no.9, 788 (2018), [arXiv:2002.00589 [gr-qc]].
- [15] S. Chen and J. Jing, Properties of a thin accretion disk around a rotating non-Kerr black hole, *Phys. Lett. B* **711**, 81-87 (2012), [arXiv:1110.3462 [gr-qc]].
- [16] S. Kazempour, Y. C. Zou and A. R. Akbarieh, Analysis of accretion disk around a black hole in dRGT massive gravity, *Eur. Phys. J. C* **82**, no.3, 190 (2022), [arXiv:2203.05190 [gr-qc]].
- [17] G. Gyulchev, P. Nedkova, T. Vetsov and S. Yazadjiev, Image of the Janis–Newman–Winicour naked singularity with a thin accretion disk, *Phys. Rev. D* **100**, no.2, 024055 (2019), [arXiv:1905.05273 [gr-qc]].
- [18] Y. Wu, H. Feng and W. Q. Chen, Thin accretion disk around black hole in Einstein–Maxwell–scalar theory, *Eur. Phys. J. C* **84**, no.10, 1075 (2024), [arXiv:2410.14113 [gr-qc]].
- [19] H. Feng, R. J. Yang and W. Q. Chen, Thin accretion disk and shadow of Kerr–Sen black hole in Einstein–Maxwell–dilaton–axion gravity, *Astropart. Phys.* **166**, 103075 (2025), [arXiv:2403.18541 [gr-qc]].
- [20] A. Liu, T. Y. He, M. Liu, Z. W. Han and R. J. Yang, Possible signatures of higher dimension in thin accretion disk around brane world black hole, *JCAP* **07**, 062 (2024), [arXiv:2404.14131 [gr-qc]].
- [21] C. Bambi, Testing black hole candidates with electromagnetic radiation, *Rev. Mod. Phys.* **89**, no.2, 025001 (2017), [arXiv:1509.03884 [gr-qc]].
- [22] J. L. Synge, The Escape of Photons from Gravitationally Intense Stars, *Mon. Not. Roy. Astron. Soc.* **131**, no.3, 463-466 (1966), [astro-ph/0301586].
- [23] J. P. Luminet, Image of a spherical black hole with thin accretion disk, *Astron. Astrophys.* **75**, 228-235 (1979), [astro-ph/0301586].
- [24] Kip S. Thorne. Disk accretion onto a black hole. 2. Evolution of the hole. *Astrophys. J.*, 191:507–520, 1974.
- [25] Z. Stuchlík and J. Schee, Shadow of the regular Bardeen black holes and comparison of the motion of photons and neutrinos, *Eur. Phys. J. C* **79**, no.1, 44 (2019), [arXiv:1904.03809 [gr-qc]].
- [26] A. Yumoto, D. Nitta, T. Chiba and N. Sugiyama, Shadows of Multi-Black Holes: Analytic Exploration, *Phys. Rev. D* **86**, 103001 (2012), [arXiv:1208.0635 [gr-qc]].
- [27] A. Abdujabbarov, M. Amir, B. Ahmedov and S. G. Ghosh, Shadow of rotating regular black holes, *Phys. Rev. D* **93**, no.10, 104004 (2016), [arXiv:1604.03809 [gr-qc]].
- [28] M. Amir and S. G. Ghosh, Shapes of rotating nonsingular black hole shadows, *Phys. Rev. D* **94**, no.2, 024054 (2016), [arXiv:1603.06382 [gr-qc]].
- [29] M. Sharif and S. Iftikhar, Shadow of a Charged Rotating Non-Commutative Black Hole, *Eur. Phys. J. C* **76**, no.11, 630 (2016), [arXiv:1611.00611 [gr-qc]].
- [30] S. W. Wei and Y. X. Liu, Observing the shadow of Einstein–Maxwell–Dilaton–Axion black hole, *JCAP* **11**, 063 (2013), [arXiv:1311.4251 [gr-qc]].
- [31] A. Abdujabbarov, F. Atamurotov, Y. Kucukakca, B. Ahmedov and U. Camci, Shadow of Kerr–Taub–NUT black hole, *Astrophys. Space Sci.* **344**, 429-435 (2013), [arXiv:1212.4949 [physics.gen-ph]].
- [32] J. C. S. Neves, Constraining the tidal charge of brane black holes using their shadows, *Eur. Phys. J. C* **80**, no.8, 717 (2020), [arXiv:2005.00483 [gr-qc]].
- [33] L. Amarilla and E. F. Eiroa, Shadow of a Kaluza–Klein rotating dilaton black hole, *Phys. Rev. D* **87**, no.4, 044057 (2013), [arXiv:1301.0532 [gr-qc]].
- [34] F. Atamurotov, A. Abdujabbarov and B. Ahmedov, Shadow of rotating non-Kerr black hole, *Phys. Rev. D* **88**, no.6, 064004 (2013).
- [35] A. K. Mishra, S. Chakraborty and S. Sarkar, Understanding photon sphere and black hole shadow in dynamically evolving spacetimes, *Phys. Rev. D* **99**, no.10, 104080 (2019), [arXiv:1903.06376 [gr-qc]].
- [36] U. Papnoi, F. Atamurotov, S. G. Ghosh and B. Ahmedov, Shadow of five-dimensional rotating Myers–Perry black hole, *Phys. Rev. D* **90**, no.2, 024073 (2014), [arXiv:1407.0834 [gr-qc]].
- [37] A. Abdujabbarov, F. Atamurotov, N. Dadhich, B. Ahmedov and Z. Stuchlík, Energetics and optical properties of 6-dimensional rotating black hole in pure Gauss–Bonnet gravity, *Eur. Phys. J. C* **75**, no.8, 399 (2015), [arXiv:1508.00331 [gr-qc]].
- [38] R. Kumar and S. G. Ghosh, Rotating black holes in 4D Einstein–Gauss–Bonnet gravity and its shadow, *JCAP* **07**, 053 (2020), [arXiv:2003.08927 [gr-qc]].
- [39] C. Liu, T. Zhu, Q. Wu, K. Jusufi, M. Jamil, M. Azreg-Aïnou and A. Wang, Shadow and quasinormal modes of a rotating loop quantum black hole, *Phys. Rev. D* **101**, no.8, 084001 (2020), [erratum: *Phys. Rev. D* **103**, no.8, 089902 (2021)], [arXiv:2003.00477 [gr-qc]].

- [40] F. Sarikulov, F. Atamurotov, A. Abdujabbarov and B. Ahmedov, Shadow of the Kerr-like black hole, *Eur. Phys. J. C* **82**, no.9, 771 (2022).
- [41] Z. Ban, J. Chen and J. Yang, Shadows of rotating black holes in effective quantum gravity, [arXiv:2411.09374 [gr-qc]].
- [42] C. Y. Yang, M. I. Aslam, X. X. Zeng and R. Saleem, Shadow images of Ghosh-Kumar rotating black hole illuminated by spherical light sources and thin accretion disks, *JHEAp* **46**, 345 (2025), [arXiv:2411.11807 [astro-ph.HE]].
- [43] X. Wang, Z. Zhao, X. X. Zeng and X. Y. Wang, Revisiting the shadow of Johannsen-Psaltis black holes, *Phys. Rev. D* **111**, no.8, 084054 (2025), [arXiv:2501.08287 [gr-qc]].
- [44] X. X. Zeng, C. Y. Yang, M. I. Aslam, R. Saleem and S. Aslam, Kerr-like Black Hole Surrounded by Cold Dark Matter Halo: The Shadow Images and EHT Constraints, [arXiv:2505.07063 [gr-qc]].
- [45] O. Yunusov, J. Rayimbaev, F. Sarikulov, M. Zahid, A. Abdujabbarov and Z. Stuchlík, Rotating charged black holes in EMS theory: shadow studies and constraints from EHT observations, *Eur. Phys. J. C* **84**, no.12, 1240 (2024).
- [46] M. Zahid, O. Yunusov, C. Shen, J. Rayimbaev and S. Muminov, Shadows and quasinormal modes of rotating black holes in Horndeski theory: Parameter constraints using EHT observations of M87* and Sgr A*, *Phys. Dark Univ.* **47**, 101734 (2025).
- [47] X. Q. Li, H. P. Yan, X. J. Yue, S. W. Zhou and Q. Xu, Geodesic structure, shadow and optical appearance of black hole immersed in Chaplygin-like dark fluid, *JCAP* **05**, 048 (2024), [arXiv:2401.18066 [gr-qc]].
- [48] S. Chen and J. Jing, Kerr black hole shadows from axion-photon coupling, *JCAP* **05**, 023 (2024), [arXiv:2310.06490 [gr-qc]].
- [49] E. T. Newman and A. I. Janis, , *J. Math. Phys.* **6**, 915 (1965).
- [50] D. Umarov, O. Yunusov, F. Atamurotov, A. Abdujabbarov and S. G. Ghosh, Plasma effects on weak gravitational lensing and shadows of Sen black holes, *Chin. Phys. C* **49**, no. 5, 055102 (2025), [INSPIRE-HEP].
- [51] W. Heisenberg and H. Euler, Folgerungen aus der Diracschen Theorie des Positrons, *Z. Physik* **98**, 714–732 (1936).
- [52] A. Sen, Rotating charged black hole solution in heterotic string theory, *Phys. Rev. Lett.* **69**, 1006–1009 (1992), [arXiv:hep-th/9204046 [hep-th]].
- [53] I.D. Novikov, K.S. Thorne, Astrophysics and black holes, in *Les Houches Summer School of Theoretical Physics: Black Holes* (1973), p. 343–550
- [54] L. G. Collodel, D. D. Doneva and S. S. Yazadjiev, Circular Orbit Structure and Thin Accretion Disks around Kerr Black Holes with Scalar Hair, *Astrophys. J.* **910**, no.1, 52 (2021), [arXiv:2101.05073 [astro-ph.HE]].
- [55] D. F. Torres, Accretion disc onto a static nonbaryonic compact object, *Nucl. Phys. B* **626**, 377-394 (2002), [hep-ph/0201154 [hep-ph]].
- [56] S. Bhattacharyya, R. Misra and A. V. Thampan, General relativistic spectra of accretion disks around rotating neutron stars, *Astrophys. J.* **550**, 841 (2001), [astro-ph/0011519 [astro-ph]].
- [57] B. Carter, Global structure of the Kerr family of gravitational fields, *Phys. Rev.* **174**, 1559-1571 (1968).
- [58] K. Hioki and K. i. Maeda, Measurement of the Kerr Spin Parameter by Observation of a Compact Object’s Shadow, *Phys. Rev. D* **80**, 024042 (2009), [arXiv:0904.3575 [astro-ph.HE]].